JMEPEG (2011) 20:1196–1205
DOI: 10.1007/s11665-010-9768-0

1059-9495/$19.00

Influence of Superheat on Microstructure and Mechanical Properties of Ductile $Cu_{47.5}Zr_{47.5}Al_5$ Bulk Metallic Glass-Matrix Composite

Alphons Anandaraj Antonysamy, Simon Pauly, Briji Kumar Dhindaw, and Jurgen Eckert

(Submitted December 16, 2009; in revised form July 12, 2010)

Generally bulk metallic glasses (BMGs) posses very less ductility and toughness at room temperature. Over the recent past years to improve up on these properties in many alloy system BMG composites have been developed. It was also reported that $Cu_{47.5}Zr_{47.5}Al_5$ BMG composite shows a very high strength together with an extensive work hardening-like behavior of large ductility around 18%. In this study, the influence of superheat on microstructure and the resulting mechanical properties in $Cu_{47.5}Zr_{47.5}Al_5$ bulk metallic glass-matrix composite alloy has been studied. The $Cu_{47.5}Zr_{47.5}Al_5$ melt solidifies into a composite microstructure consisting of crystalline precipitates embedded in an amorphous matrix. The crystalline phase consists of B2 CuZr (cubic primitive with CsCl structure) with a small amount of monoclinic CuZr martensitic structure embedded in an amorphous matrix. The volume fraction of crystalline phases varies with melting current as well as position along the length of the as-cast rod, depending on the local cooling condition. The volume fraction and the distribution of the crystalline precipitates are heterogeneous in the amorphous matrix. Room temperature uniaxial compression tests revealed high yield strength ranging from 796 to 1900 MPa depending upon the volume fraction of the crystalline phases present. The presence of the dendritic B2 CuZr significantly improved the ductility. The BMG composites show a pronounced plastic strain up to 14% for the higher volume fraction of crystalline phase.

Keywords amorphous, bulk metallic glasses, composite, $Cu_{47.5}Zr_{47.5}Al_5$, fracture surface, mechanical properties, microstructure

1. Introduction

In the past few years interest in the bulk metallic glasses (BMGs) has increased because of the possibilities to cast larger thickness at a relatively lower cooling rates, typically in Zr- and Cu-based alloys ($<$1-10 K/s) (Ref 1-3). Their mechanical properties have been investigated intensively with respect to the commercial applications (Ref 4). The major advantages of BMGs in general are high strength, low elastic modulus with good wear properties (Ref 3, 5). However, the BMGs fracture catastrophically and the process involves very little amount of overall plastic ductility. The lack of macroscopic plasticity is mainly due to the shear softening phenomenon due to high localized shear. Once a shear instability forms during deformation, it will be more prone to further shearing due to free volume generation and a decrease in viscosity accompanying it. Thus, the already deformed region continues to deform and the glass fails catastrophically along a single shear band. In BMGs, failures have majorly occurred at an angle approximately 45° which is the plane of maximum shear in a shear mode. Dislocations in crystals are responsible for plasticity and hardening. Primarily due to the absence of crystalline phases and dislocation-based deformation, BMG shows poor plasticity.

In order to overcome the limited plastic deformability of metallic glass, several composites have been developed by incorporating nanoscale/micrometer sized precipitate of crystals in a BMG amorphous matrix. In turn, these crystalline phases introduce heterogeneity and the resulting BMGs with crystalline phases called "BMG composites." There are different approaches to increase the plasticity in BMGs and, can be classified into (i) ex situ composites: introducing the quasi-crystalline or nanocrystalline reinforcement into a glassy matrix for example in the form of particles or fibers and (ii) in situ composites: crystal phase formed from the melt during the solidification containing either particle or ductile dendritic phase reinforcements (Ref 6-11). Significant improvements in ductility have been achieved in many systems by hindering the propagation of shear band at crystalline precipitate. Crystalline precipitates increase the plasticity through multiplication, branching, and restriction of the shear band and this has been studied and reported for Zr-Ti, Ta-Cu-Ni-Al, Pt-Cu-Ni-Al, Cu-Zr-Al systems (Ref 12, 13).

The Cu-Zr system was found to have an unexpected high glass-forming ability (GFA) even for a binary alloy with a critical casting thickness of up to 2 mm (Ref 14-16). It has been observed that the GFA of Cu-Zr binary alloy improved

Alphons Anandaraj Antonysamy, IFW Dresden, Institut für Komplexe Materialien, Postfach 27 01 16, 01171 Dresden, Germany and Department of Mechanical Engineering, Indian Institute of Technology Ropar, Punjab 14001, India and Manchester Materials Science Centre, University of Manchester, Manchester M1 7HS, UK; **Simon Pauly**, IFW Dresden, Institut für Komplexe Materialien, Postfach 27 01 16, 01171 Dresden, Germany; **Briji Kumar Dhindaw**, Department of Mechanical Engineering, Indian Institute of Technology Ropar, Punjab 14001, India; and **Jurgen Eckert**, Technical University Dresden, Institut für Werkstoffwissenschaft, 01062 Dresden, Germany. Contact e-mail: dhindaw@metal.iitkgp.ernet.in.

drastically by the addition of Al (Ref 16). The high tendency of the Cu-Zr-Al system to vitrify can be attributed to the fulfilment of the three empirical criteria. At first, the present system is a multi-component system; secondly, the ratio of atomic radii of Cu, Zr, and Al are all greater than 12% ($r_{Al} = 0.143$ nm, $r_{Cu} = 0.128$ nm, $r_{Zr} = 0.160$ nm); and thirdly, the elements all have the large negative heats of mixing. The heat of mixing of Al and Zr is about two times higher than that of Cu and Zr ($\Delta_{mix}H$ (Cu-Zr) = −23 kJ/mol, $\Delta_{mix}H$ (Al-Zr) = −44 kJ/mol) (Ref 17). Especially the Cu-Zr-based multicomponent BMG composites reinforced with a dendritic phase, exhibit promising mechanical properties (Ref 15, 16). The suitable composition of the alloy to ensure high GFA as well as the size, shape, distribution, and volume fraction of the crystalline phases are much more important to tailor the mechanical properties. It was reported by Z.W. Zhu et al. that the $Cu_{47.5}Zr_{47.5}Al_5$ BMGs bearing some nano-crystals with the size of 2 to 7 nm exhibits a good plasticity. This indicates that the microstructure of the BMGs is closely affected by the solidification conditions and, the controlling over solidification condition could improve the plasticity of BMG composites (Ref 18). Recently, Das et al. has reported that the ternary composition of $Cu_{47.5}Zr_{47.5}Al_5$ BMG composite shows a pronounced ductility and further exhibits a work hardening-like behavior. It was reported that a glassy rod of diameter 2 mm yields a compressive strength of up to 2265 MPa together with plastic strain of about 18% (Ref 14-16, 19, 20). The crystalline phases detected in the composites are the B2 CuZr as well as the CuZr martensite (Ref 16, 19, 20). Because of the interesting mechanical properties of this particular system of $Cu_{47.5}Zr_{47.5}Al_5$ BMG composites, this study investigates the influence of the casting conditions (influence of super heat of the melt) on microstructure and the resulting mechanical properties on $Cu_{47.5}Zr_{47.5}Al_5$ BMG composite forming alloy.

2. Experimental Details

A pre-alloyed ingot with nominal composition of $Cu_{47.5}Zr_{47.5}Al_5$ was prepared from pure elements (purity > 99.99 wt.%) by arc melting in a titanium-guttered argon atmosphere. The ingots were re-melted several times to achieve homogeneity in the final composition. The pre-alloy were melted in an arc melter (Edmund Bühler) and solidified into rod shape by an in situ copper mold suction casting facility attached to the arc melter. A copper mold with a cavity of diameter 2 mm was employed for all rods. The plasma arc is very intense so the ordinary pyrometer cannot be used to measure the temperature of the melt directly. Since there is no direct control over the temperature during the casting process due to the Ar-plasma, to change the temperature of the melt, the melting current is varied which in turn directly varies the superheat of the melt. The alloys were melted and cast as a rod using melting currents in two different ranges. Series 1 ($100 < I < 220$ A, with the specific melting current of 100, 130, 180, and 200 A), and series 2 ($150 < I < 260$ A, with the specific melting current of 150, 220, and 260 A). As there might be slight differences in properties due to the drastic variation in the melting current in series 2, the two sets of samples are discussed separately throughout the course of this study.

In order to identify the structure of the as-cast rods, disks of thickness about 50-100 μm were prepared and, characterized by *x-ray diffraction* in transmission geometry in a *STOE STADI P* (λ (Mo Kα) = 0.70932 Å). Microstructural analysis was carried out using (i) *Zeiss Axiophot* optical microscopy, (ii) *Zeiss DSM 962* and, (iii) *Hitachi TM1000* with the accelerating voltage of 20-25 kV and a working distance of 10-15 mm. Composition analysis was carried out by EDX technique using (iv) *Phillips XL 30 FEG SEM* equipped with EDX unit. In addition to this EBSD facility in the Phillips XL 30, FEGSEM was also used to study the nature of crystal structure of the cast rod. The analysis of thermal properties was carried out using a *Perklin Elmer DSC7* (*Differential Scanning Colorimetry*) at a heating rate of 20 K/min. The Elastic modulus of the cast rods was determined through measurement of ultrasonic sound velocity using *Panametrics 25DL plus* (*Olympus*). The density of the sample which is used here to determine the Youngs modulus was evaluated on the basis of Archimedes principle. *Leco M400-G2* hardness tester was used to measure the *Vickers hardness*. Finally, the mechanical properties of the as cast rods were studied under compressive loading in *Instron 5569* testing machine using a constant strain rate of about 1 E-4 s-1. The aspect ratio of the compressive samples was in the range 1.5-2.

3. Result and Discussion

3.1 Structural Analysis

The diffraction patterns of series 1 and 2 (Fig. 1) show a sharp reflection superimposed on a broad maximum, pointing toward a composite microstructure consisting of a glassy and at least one crystalline phase. Generally, the intensities of Bragg peak increase with increase in the volume fraction of crystalline phases (Ref 17). The diffracted patterns were analyzed and Bragg reflections were found to correspond to CuZr crystalline phase (space group: Pm-$3m$), the so called B2 CuZr phase with small amount of monoclinic CuZr martensite (space group: $P2_1/m$, and Cm (Ref 14-16, 18-21). Since, the sample for XRD had been taken from the end of compression test piece; the formation of the martensitic structure most likely is due to the stress-induced transformation during deformation. For the above analysis, the lattice constants were obtained from Rietveld refinement. The lattice parameter varied from 3.260 to 3.266 Å for the series 1 for the different melting conditions (different melting currents). This is in good agreement with the value reported for the $Zr_{48.5}Cu_{46.5}Al_5$ alloy (Ref 17). Figure 1(b) shows the XRD pattern of series 2 samples obtained in the as cast condition for three different melting conditions. The diffraction patterns of the rods cast with a melting current of 150 and 260 A show intense Bragg reflections of B2 CuZr superimposed on a broad maximum caused by the amorphous structure. But, reflections from martensitic phase could not be clearly observed since the sample is directly taken from the as-cast rods when compared to the range of samples analyzed in series 1. However, at a melting current of 220 A, the diffraction pattern shows that the samples are nearly complete amorphous.

There is no trend observed with respect to the variation in melting current in the range of melting conditions of series 1. In order to study the homogeneity of the cast rods, additional XRD analysis had been carried out at different positions along the length of the rod as shown in Fig. 2. It is evident from the intensity of the peaks; the crystals were formed over the whole length of all the rods. Showing a heterogeneous distribution of

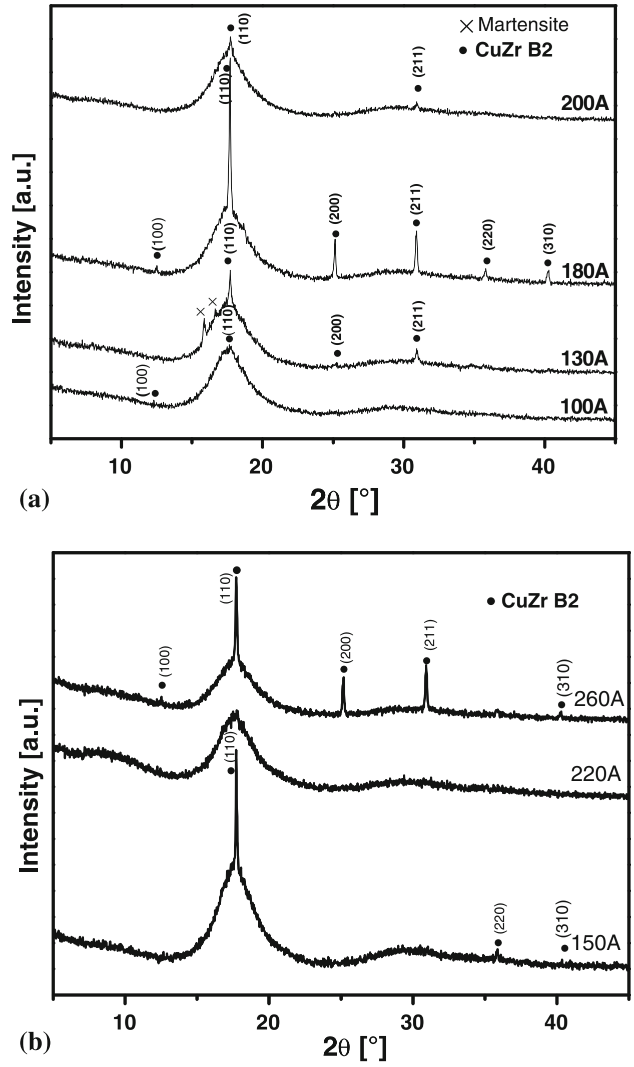

Fig. 1 (a, b) XRD pattern of series 1 and series 2, respectively, in the as-cast condition

crystals and no clear trend with cooling rate is apparent. Thus, the crystalline phase is in-homogeneously distributed throughout the length of an every rod (Fig. 2a-d). This can be judged from the intensities of B2 CuZr reflections varying at different sections of the as-cast rod. The sample cast with a melting current of 130 A shows a strong peak at 18.5° which corresponds most likely to CuZr martensite. Its relatively strong intensity could be explained by a preferred orientation of the crystals in the matrix.

The microstructure consists of agglomerated round particles of dark contrast phase embedded in a bright matrix (as shown in Fig. 3) under the optical microscopy. The dark phase in the micrograph indicates the presence of crystalline phase the glassy matrix. The size of the spherical-shaped precipitates varies from 10 to 210 μm. The volume fractions of the crystalline phases vary with respect to the melting current. However, there is no trend observed with respect to the variation of melting conditions (Fig. 3; Table 1). It would normally be expected that more crystalline phases should form at the top of the rod as compared to the bottom, since the liquid at the top will not solidify for long time. However, the observed results contradict this. Higher amount of precipitates are observed in the bottom than that the top in the cast rod of 100 and 130 A (Table 1). This implies that the local cooling rate is important and, this significant variations in local cooling rate lead to a heterogeneous distribution of crystals. Some of the precipitates are found at the outer edge of the cast rods and this pattern of formation of microstructure may be due to the improper wettability of the mold or may be due to the gas entrapment, causing a slower heat removal at the surface leading to formation of higher amount of crystalline phases in the amorphous matrix. As indicated by XRD results, the large-sized crystals are in-homogeneously distributed throughout the length of a single rod.

In the series 2, to confirm whether melting current of 220 A is optimum melting current for a fully amorphous BMG, additional slices were prepared along the length and investigated. The XRD patterns of additional sample also show a completely amorphous structure at the melting current of 220 A (Fig. 2e). This may be due to the fact that a melting condition of 220 A is the optimum current providing the optimum melting temperature to form a completely amorphous structure from range of melting conditions and, Fig. 3(b) shows the micrograph of range of melting current obtained from the series 2 cast rods. The volume fraction of crystals in 220 A observed to be almost nil (Table 1) as it was stated earlier in the XRD pattern that the rod cast with a melting current of 220 A shows almost a fully amorphous phase when compared to the other two samples. The crystalline phase at the edge (arrow show the visible phase in the 260 A cast rod), might be due to the variation of local cooling condition resulting in higher volume fraction of crystalline phase. Samples with 260 A in series 2 also show a presence of the dendrites (inset in Fig. 3b in 260 A).

3.2 Microstructural Analysis

In order to reveal possible substructures in the dark and the bright contrast regions of the microstructure obtained from the optical microscopy, SEM analysis was done at higher magnification. The different kinds of microstructural features have been revealed at higher magnifications as, (i) a bright and featureless amorphous matrix, (ii) dark precipitates which do not show any substructure, (iii) dark precipitates which contain a dendritic substructure in some regions, and (iv) Single dendrites are found in the matrix (as shown in Fig. 3(b) for 260 A).

SEM micrographs show almost a featureless bright matrix with small amount of precipitates embedded in matrix. Some of the precipitates do not show any substructure in SEM in the BSE mode (Fig. 4a) like the ones in the top part of the rod cast at a melting current of 100 A. In order to characterize these featureless particles, EBSD analysis was carried out on this particular feature. Kikuchi lines (Fig. 4b) were detected and confirm the crystalline nature of these precipitates. The Kikuchi patterns could be indexed assuming the B2 CuZr structure through the use of lattice parameters determined by Rietveld refinement by the XRD analysis. Figure 4(b) shows Kikuchi patterns of the precipitates and Fig. 4(c) shows the indexing superimposed on the measured pattern. From the EBSD experiments, it could be concluded that the B2 CuZr phase forms relatively large spherical crystals heterogeneously distributed throughout the length of the rod. Kikuchi lines stemming from the B2 CuZr phase were also detected in the precipitates occurring in all the other rods cast with different melting currents.

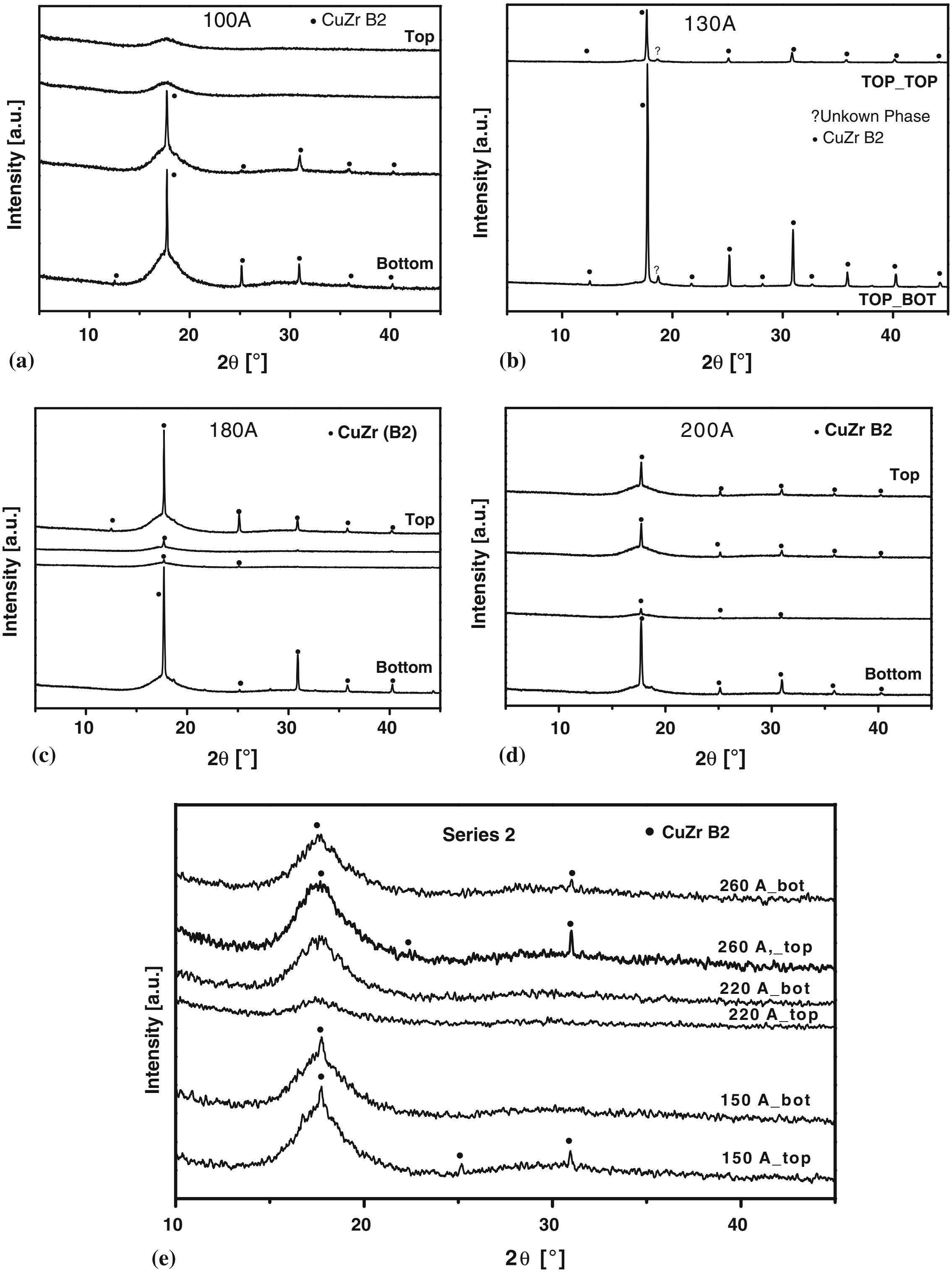

Fig. 2 (a-d) Distribution of crystalline phases across the length for different melting currents in series 1 and (e) shows XRD pattern of top and bottom section of the series 2 cast rods

Majority of the precipitates show a pronounced dendrite substructure visible within dark contrast (Fig. 5). For example, in the cast rod of 130 A (both the bottom and the top parts) shows primarily the dendritic substructure, which are distributed non-uniformly as the dark contrast region near the outside edge of sample. The size of the dendrites near the edge was about 0.5 μm, whereas the particles which were present at the center of the rod also showed a pronounced dendritic structure with dendrite size of about 2 to 3 μm due to the variation in cooling rate between the center (lower) and the outside edge (higher). Between the dendrite arms a eutectic structure could be observed (Fig. 5b) in the BSE mode. However, it's fine

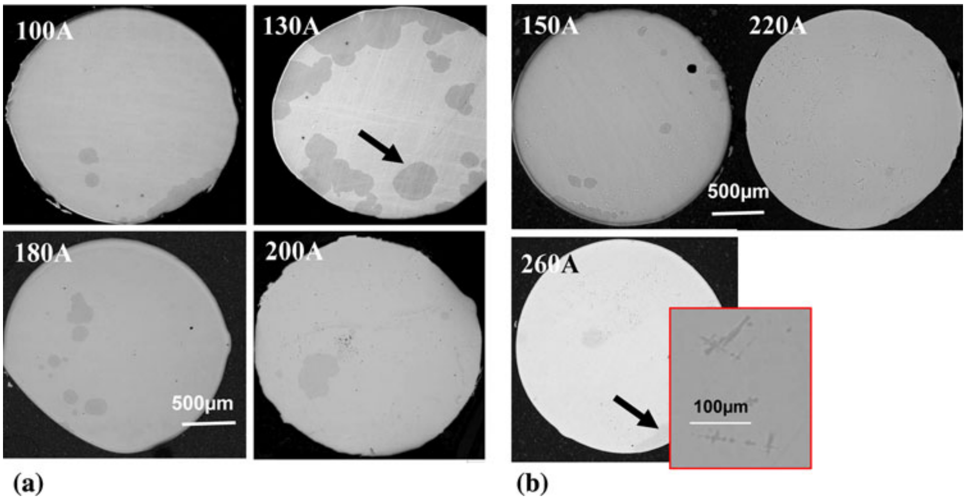

Fig. 3 (a, b) Micrograph of series 1 and series 2, respectively, under optical microscope. Inset in the 260 A of (b) shows a presence of single dendrites under optical microscope.

Table 1 The list of melting conditions with volume fraction of crystalline phases measured by optical microscopy and, thermal properties obtained though DSC measurement

Melting current, A	Location	Crystalline vol. fraction by OM, %	T_g, K	T_x, K	ΔT_x, K	$T_{rg} = (T_g/T_{liq})$	$\Delta_{cryst}H_m$, J/g
Series 1							
100	Top	0.0	704	757	53	0.58	−62.9
	Bottom	4.7	703	757	54	0.58	−57.4
130	Top	4.7	701	757	56	0.58	−55.7
180	Top	49.5	702	759	57	0.58	−51.2
	Bottom	10.7	707	759	52	0.59	−54.6
200	Top	4.2	704	759	55	0.58	−60.7
	Bottom	7.6	705	760	55	0.58	−61.7
Series 2							
150	Top	…	710	765	55	0.59	−47.0
	Bottom	…	707	764	57	0.58	−50.8
220	Top	…	706	765	59	0.58	−52.1
	Bottom	…	703	762	61	0.58	−52.4
260	Top	…	708	766	58	0.59	−49.0
	Bottom	…	702	762	60	0.58	−49.0
Series 2 additional samples							
150	Center	4.6	719	788	69	0.59	−57.4
220	Center	0.7	720	789	69	0.59	−61.0
260	Center	9.6	705	768	63	0.58	−47.6

lamellar structure could not be resolved even at high magnifications (×10000) due to the higher cooling rate associated with the formation of BMG. EDX analysis was done on the dendritic and interdendritic region as shown in the Fig. 5, to reveal the compositional difference between the regions and the corresponding results are tabulated in Table 2. There is no significant difference in the composition between the matrix and the precipitate at lower magnifications. But substructure at higher magnification reveals the variation of composition in the dendritic and interdendritic eutectic regions. The Al content of the eutectic (6.5 at.%) is about two times higher than that of the dendritic phase (3.8 at.%). This obviously happens due to the micro-segregation induced at these higher cooling rates.

In the present system ($Cu_{47.5}Zr_{47.5}Al_5$), excess Al of 5 at.% introduced into the equiatomic CuZr system, changes the solidification behavior of alloy completely (Ref 22). Once the temperature drops from 1215 °C, the CuZr primary dendrites start to grow form nuclei and the presence of excess solute (Al) substitutes the Cu atoms in equiatomic CuZr primary dendritic phase since the difference in atomic radii between the Al and the Cu atoms is less when compared with Al and Zr, and the second reason is high negative enthalpy of mixing between Al and Zr when compared to the Al and Cu. The rejected Cu atoms from the solidification front increase the Cu content in the remaining liquid (composition of liquid, shifted toward the left side from the equiatomic) and forms eutectic compound (alternate layer of $Cu_{10}Zr_7$ and $CuZr_2$ at room temperature) as per the phase diagram (Ref 22, 23). Since the cooling rate is very high in the copper mold, one can expect a high temperature eutectic structure (alternate layer of $Cu_{10}Zr_7$ and CuZr) to be retained at room temperature. Since cooling rate is very high even at higher magnification the lamellae structure in the eutectic is not revealed. In summary, one would expect the

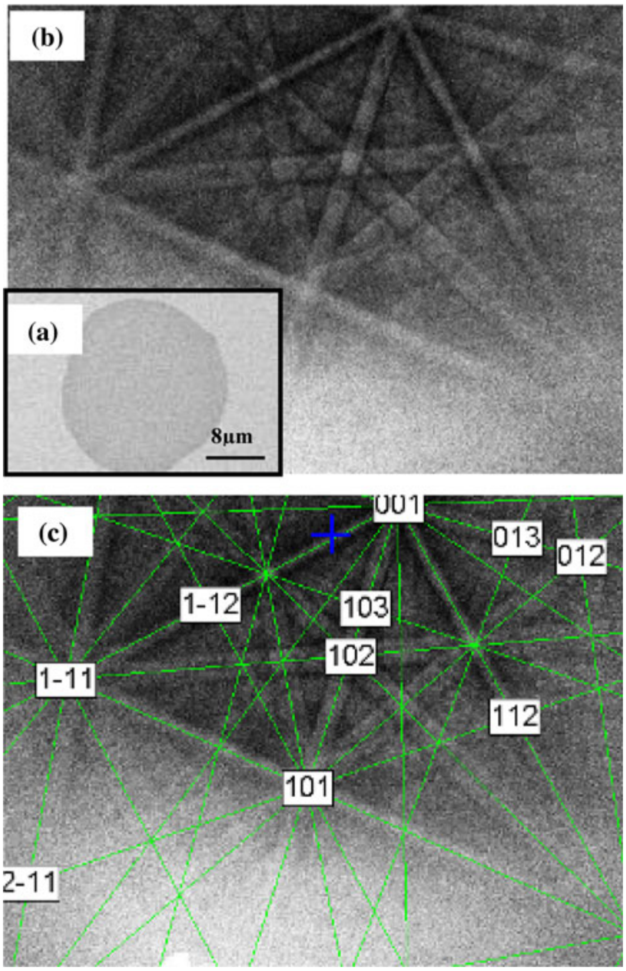

Fig. 4 (a) Micrograph of 100 A cast rod (bottom section) under SEM (BSE), (b) EBSD Kikuchi pattern of the dark featureless region (a), and (c) Kikuchi pattern superimposed with standard Kikuchi band lines of B2 CuZr phase

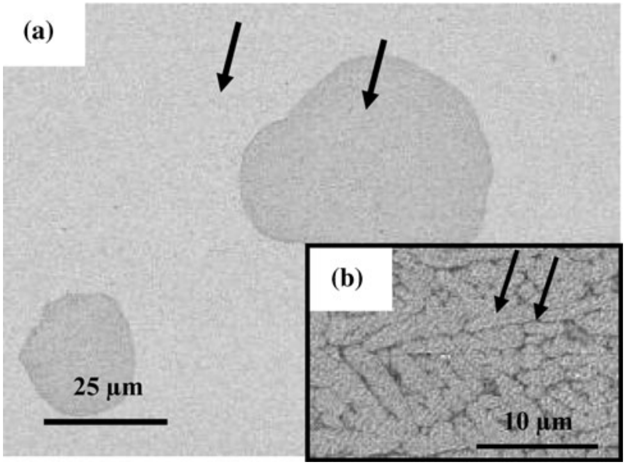

Fig. 5 (a) SEM micrograph (BSE) of 130 A cast rod (bottom) at low magnification, (b) the presence of dendrites substructure inside the precipitate at higher magnification. The marked locations indicate the spots, where the composition has been analyzed by EDX

Table 2 EDX data for the specific melting current of $Cu_{47.5}Zr_{47.5}Al_5$ 130 A cast rod

Location	Region of the microstructure	Al, at.wt.%	Cu, at.wt.%	Zr, at.wt.%
130 A bottom	Matrix	3.64	48.05	48.31
	Precipitate	3.66	47.22	49.12
	Primary dendrites	3.78	45.98	50.24
	Eutectic	6.56	48.80	44.64

primary dendrite with a depleted Al content and the interdendritic eutectic regions with enriched Al content and the EDX analysis clearly reveals the same for the melting current of 130 A cast rod. The primary dendritic phase has the Al content of 3.8 at.% and the eutectic regions are with 6.5 at.% Al.

The dark single dendrites (inset in Fig. 3b in 260 A) show a Al content of about 9.5 at.%, and the bright matrix showed a Al content of about 4.0 at.% Al. Thus, the brighter glass matrix regions are depleted in Al and the dark regions are enriched with Al. The single dendrites might have formed directly from the liquid metal through nucleation and growth, but would have stopped their growth due to very high local cooling associated. At the high rates of cooling the substructures and the eutectics are very difficult to resolve. Thus, the issue has been left without any speculative discussion.

3.3 Thermal Properties

Figure 6(a) and (b) shows the differential scanning calorimetry traces from the top section of the cast rods with different melting currents with a heating rate of 20 K/min. All the specimens show a distinct glass transition (T_g) at about 705 K and a sharp crystallization peak (T_x) at 760 K as shown in Table 1 (Ref 16, 20, 21, 23, 24). The enthalpy of crystallization ($\Delta_{cryst}H_m$) is very sensitive to the amount of the crystalline phase present in the sample. The higher the crystalline volume fraction, the lower the heat released by the sample during crystallization process. The enthalpy of crystallization is about 62.9, 55.7, 51.2, and 60.7 J/g for the top section of the cast rods prepared at melting currents 100, 130, 180, and 200 A, respectively. The rods cast at 100 and 200 A contain a relative higher volume fraction of the glass phase than the rods cast with melting conditions of 130 and 180 A currents (Table 1 shows the volume fraction of glassy phase for different cast samples). Series 1 and 2 cast rods reveal a large scattering in the enthalpy of crystallization and resulting volume fraction of the crystals along the length of the rods also varies, respectively. This was also confirmed by the XRD and the optical microscopy analysis. This may be attributed to the difference in the volume fraction of CuZr B2 phase along the length of the cast rods that seems to be strongly depends on the local cooling conditions and, it is expected to be influenced by the presence of cavities and improper wettability. Meanwhile, it could be noted that lower and higher meting currents in series 2 show a higher volume fraction of crystals and the XRD results were perfectly matching with the findings of variation of crystalline phase content as shown by DSC results. Melting condition of 220 A currents shows a complete amorphous glassy nature.

3.4 Mechanical Properties

The mechanical properties of any BMG matrix composites depend upon the amount of volume fraction of crystals,

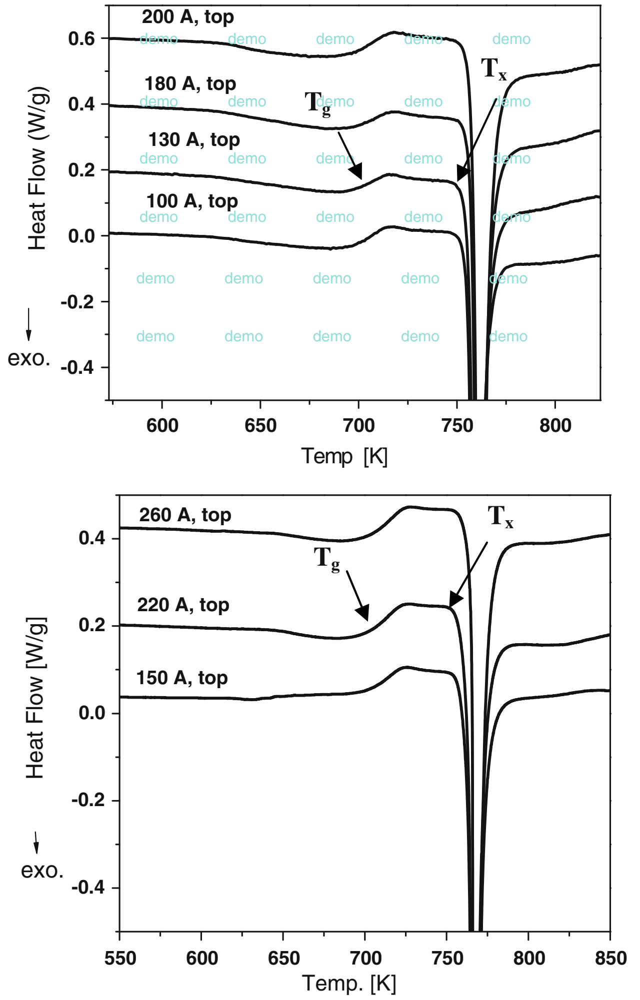

Fig. 6 (a, b) DSC traces of top section for different casting conditions at constant heating rate of 20 K/min for series 1 and series 2, respectively

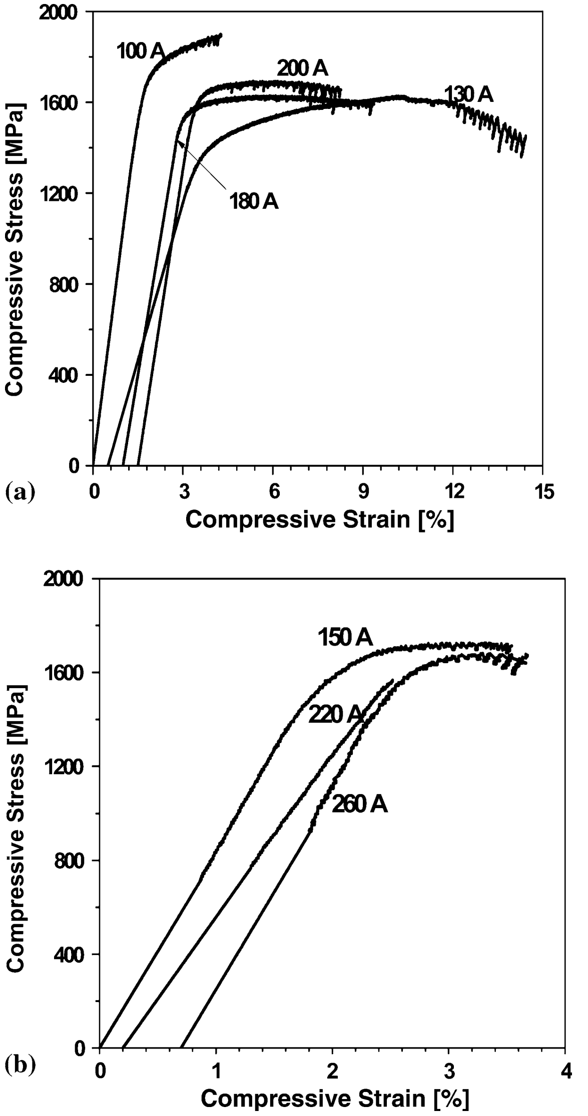

Fig. 7 Uni-axial compressive stress-strain curves of (a) series 1 (top section) and (b) series 2 at room temperature

properties of the different phases present, size and the distribution of the crystals (Ref 21, 25). The stress-strain curve of series 1 has been shown in Fig. 7(a) and the corresponding results are tabulated in Table 3. All the cast rods show the G/B ratio within the range 0.274-0.305 (shown in the Table 3) and it is well below the threshold region of 0.42, i.e., the value of G/B which is lesser than the threshold value of 0.42 predicts, the properties of BMG composite as tough and ductile (Ref 26). The Elastic constant values are consistent in both the series, and the variation in the crystalline volume fraction described in microstructure does not seem to significantly influence the elastic constants to a greater extend. The sample cast at 130 A (top) shows large plasticity with a fracture strain of about 14% with low yield strength of about 796 MPa in comparison with the other samples. The reason for this reduction in the yield strength is due to the presence of higher amount of B2 CuZr crystals. Unfortunately, the mechanical behavior of the pure CuZr B2 phase is unknown; however, the hardness of the crystals can be used as an indication for the yield stress: $HV = 3\sigma_y$. As the hardness of the crystalline phase (Avg. 536 HV0.5) is lower than the hardness of the matrix (Avg. 701 HV0.5), and the yield strength of the composites having a large volume fraction of crystals should be low. Furthermore, along with the improved plasticity (11%), a pronounced work hardening behavior was observed as if the regular polycrystalline materials and it is mainly due to the presence of large amount of inhomogeneously distributed crystalline precipitates (Ref 16). The serrations in the stress-strain curves are mainly due to solute-dislocation interaction phenomenon reported in Ref 25.

The elastic-plastic behavior is thus strongly influenced by the volume fraction crystalline precipitates in the amorphous matrix. The large plastic strains, Young's modulus, and high yield strengths are in good accord with the values reported by Das et al. (ductility of 18%) for the same composition (Ref 16). The stress-strain curve of series 2 has been shown in Fig. 7(b) and the corresponding results are tabulated in Table 3. In series 2, 220 A melting current shows almost no plasticity in contrast to the 150 and 220 A. This is expected as the XRD and DSC measurements prove that this sample is fully glass. Apparently, the glass is prone to a catastrophic failure not showing any or only little plastic deformation. The 150 and 260 A cast rods have a higher volume fraction of the crystals and therefore

Table 3 Summary of compression test results and Elastic constants (determined using ultrasonic measurements) of as cast $Cu_{47.5}Zr_{47.5}Al_5$

Current rate, A	Location	$\sigma_{y(0.2\%)}$, MPa	ε_y, %	σ_m, MPa	ε_f, %	Poisson's ratio	*E*, GPa	*G*, GPa)	*K*, GPa)	*G*/*K*
Series 1										
100	Bottom	1618	1.66	1901	4.27	0.373	88.4	32.2	116.1	0.277
	Top	1399	1.51	1804	2.83	0.361	94.4	34.5	112.7	0.305
130	Bottom	1311	2.93	1628	13.94	0.374	88.5	32.4	117.4	0.278
	Top	796	2.83	1468	10.97	0.374	89.1	32.4	117.5	0.276
180	Bottom	1527	2.04	1632	8.37	0.374	88.3	32.1	116.6	0.275
	Top	1545	1.87	1739	7.3	0.374	89.0	32.5	116.9	0.278
200	Bottom	1555	1.88	1695	6.76	0.374	87.9	32.0	116.4	0.274
	Top	1427	1.88	1684	6.01	0.374	89.8	32.7	118.2	0.277
Series 2										
150	Center	1580	42.01	1729	3.55	0.373	89.7	32.8	117.6	0.278
220	Center	1574	2.52	1574	2.52	0.372	89.9	32.8	116.5	0.280
260	Center	1608	2.43	1678	3.38	0.373	89.8	32.7	117.4	0.279

show lower yield strengths but a significantly higher fracture strains (~4%).

As it was reported by Zhu et al. (Ref 18) in the suction casting method, the local structural-ordering atomic clusters can be present when the high temperature melt is suddenly sucked into a high cooling copper mold and thus freezes the clusters into the whole melt when it solidifies. This results in lot of inhomogeneity of the castings in series 1, whereas the mechanical properties in series 2 seem to vary in a systematic way. When the melting current is about 150 A, the melt is just heated above the liquidus temperature. This temperature might not be sufficient to completely dissolve nuclei (unmelted prior clusters) which assist the formation of crystals during cooling. The melting current of 150 A (low temperature) causes a local structural-ordering clusters exist in the glass-forming melt as such (Ref 18, 27-29) and, they act as nuclei (pre-existing undissolved clusters) during the solidification and leads to the formation of crystalline phase in the amorphous matrix. The local structural-ordering clusters are stable only at low temperatures. As the temperature is increased, the atoms in the cluster dissociate. The local structural ordering clusters will fully dissolve at a high temperature (Ref 30) possibly when the melting current is 220 A, and the dissolution of the clusters leads to a monolithic amorphous structure. Thus, melting current of 220 A might be optimum temperature, where all the nuclei potentially causing homogeneous nucleation and growth during rapid solidification are destroyed. Yet, the heat content of the melt is still low enough to bypass the crystalline nose during solidification at the given cooling rate. The result is a fully glassy structure at room temperature. Whereas when the melting current reaches 260 A, it is expected that the large amount of heat in the melt cannot be removed under a given cooling conditions without avoiding the partial crystallization of the melt.

3.5 Fractography

It was observed that the microstructure seems to be mainly dependent on the local cooling rate that is found to change along the length of the as-cast rods and the outcome was a heterogeneous distribution of crystals over the whole length of a rod. Consequently, one would expect different fracture mechanisms for the samples with different crystalline volume fractions (Ref 14-16). All the fracture surfaces were investigated. However, here only the "extremes" found in terms of plasticity in the compression tests will be discussed irrespective of the two ranges of the melting currents (series 1 and 2). The fracture surface analysis shows a significant change in the appearance of the fracture surfaces between the very ductile (~14% strain with higher amount of crystalline phase in 130 A cast rod) and brittle (1 to 2% strain with almost no plastic ductility in 220 A cast rod) samples and this will be discussed briefly.

Specimen shears approximately at an angle of 45° to the loading axis. Mixtures of river- and vein-like patterns with higher number of shear bands are observed on the fracture surfaces of the ductile specimen. Next to smooth featureless regions, which could be described to lie in "valleys," a vein- and a river-like pattern (Fig. 8a) are well developed (Ref 14-16, 18-21). In Fig. 8, the elliptical circle shows the vein-like pattern and this uniform arrangement follows the flow direction in the shear plane. It may indicate presence of partial melting and consecutive solidification process during fracture and this suggests that the temperature of the material rises above the melting temperature during the fracture. When fracture occurs during compression, the stored energy has to be dissipated somehow within the material and this can be obtained in the form of heat which causes local melting of the material and the resulting flow lines on the fracture surface (Ref 19-21, 31-34). The intermittent smooth regions could have formed during fast crack propagation in the glassy matrix. They are elongated in the direction of the shear. Near the transverse crack deep river-like patterns are observed. The final facture surface is rather rough indicating that next to the shear stress the normal stress also acts on the fracture plain. Here, solidified melt droplets are also found on the fracture surface. Many shear bands can be seen on the superficial surface of compressed rods as shown in Fig. 8(a). The higher number of shear bands are mainly due to the presence of large number of heterogeneously distributed crystalline precipitates. These crystalline precipitates multiply and deflect the shear crack propagation and also increase the branching of cracks. One can clearly observe that shear bands with two different orientations intersect and sharp edges are created at the intersection (arrows in Fig. 8b). A high density of shear bands associated with vein-like pattern results in a more homogenous strain distribution in glass matrix composites causing high plasticity (fracture strain of about 14%). It is found that the area of the vein-like pattern increases as the

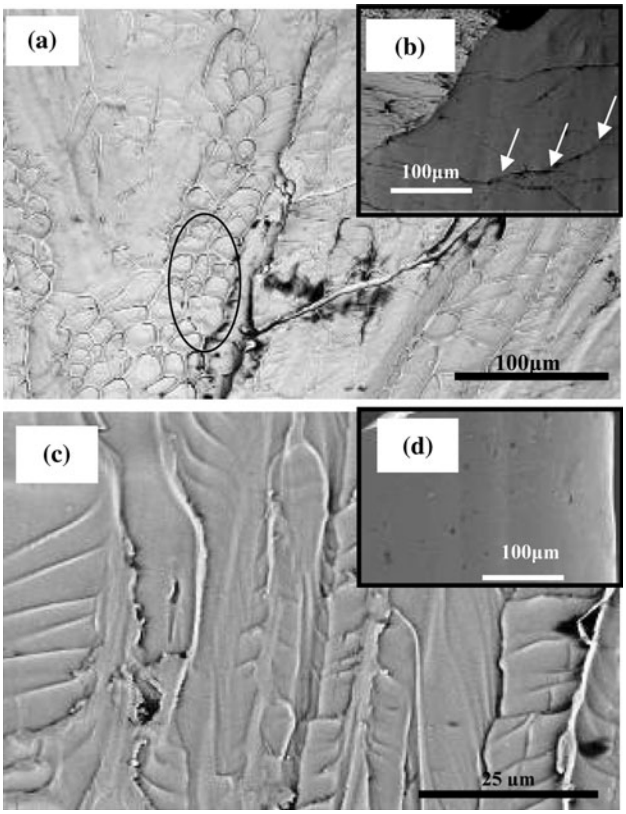

Fig. 8 (a) The fracture surface of 130 A cast rod (more ductile specimen) under SEM (SE) showing the vein-like pattern, river-like with lateral crack, (b) SEM image of different orientations of the cracks intersecting each other on the fracture specimen superficial area of (a); (c) The fracture surface of 220 A cast rod (almost nil ductility) under SEM (SE) showing heavy river-like pattern, and (d) shows the superficial area of specimen (c)

number of shear band as well as the macroscopic plastic strain (and toughness also) increases (Ref 34-36).

It was observed that the 220 A cast rod is nearly fully glassy and it does not show any plastic strain before failure when compared to all the other cast rods. The specimen shears almost nearly at an angle of 45°. The sample is fractured only on the major slip plane and almost no or very little plastic strain is observed. Hardly any shear bands were observed on the superficial surface (Fig. 8b). This implies that the sample is more brittle in nature due to the absence of multiple shear bands on superficial surface in the absence of crystalline precipitates (Ref 34-36). This indicates that the shear bands are the carriers of plastic deformation, and higher the shear band density higher the macroscopic plastic strain. Whereas the medium ductile specimens show an equal amount of vein- and river-like pattern together with a moderate amount of shear bands on their surfaces.

4. Summary

The microstructure consists of B2 CuZr phase with a small amount of monoclinic CuZr martensite embedded in an amorphous matrix. The volume fraction of crystalline phase varies with melting current as well as along with the length of the as-cast rod, depending on the local cooling condition. Compositional fluctuations are observed in different phases of the $Cu_{47.5}Zr_{47.5}Al_5$ composites. The presence of chemical fluctuation and structural heterogeneities in the $Cu_{47.5}Zr_{47.5}Al_5$ BMG is believed to contribute to the large plasticity and work hardening-like behavior during deformation. Under compressive loading, the yield strength strongly scales with the glassy volume fraction ranging from min. 796 MPa to max. 1905 MPa. The ultimate strength values vary between 1574 and 2025 MPa and apparent work hardening behavior has been observed from 2% to a large plastic strain up to 14%. Young's modulus: around 88-97 GPa with Poisson's ratio of around 0.361 to 0.374 has been observed in the as cast condition. And, the G/K ratio was observed to lie in the range 0.275-0.305, which is well below the critical limit of ductile to brittle transition limit.

The fracture morphology consists of a vein-like pattern, intermittent smooth regions and a river-like pattern. The vein-like pattern is the more pronounced in the larger plastic strain specimens with higher density of slip lines (on the surface). Medium ductile specimens show an equal amount of vein- and river-like pattern with a moderate amount shear bands (on the surface). The brittle specimens show a pronounced river-like pattern with very few or almost a no shear band. No obvious trend has been observed with respect to casting condition, i.e., melting current (superheat) in terms of microstructure and mechanical properties in series 1, whereas series 2 shows a systematic variation with respect to the melting current, the reason could be the higher variation of melting current used in series 2 cast rods.

Acknowledgments

We would like to thank Jayanta Das, Utta Kühn, Shankar Venkataraman, Lakshmi Lavanya Parimi, Amitesh Kumar and Mahesh Emmi for technical assistance and stimulating discussions. A.A. Antonysamy is also grateful for the financial support provided by the "DAAD - IIT Kharagpur Sandwich Program" for his stay at IFW-IKM, Dresden Germany and, special thanks to Markus Rimmele and Benedikt Romberg for their continuous support from DAAD office, Dresden during the whole period of study in Germany.

References

1. A. Inoue, T. Zhang, and T. Masumoto, Zr-Al-Ni Amorphous Alloys with High Glass Transition Temperature and Significant Supercooled Liquid Region, *Mater. Trans.*, 1990, **31**, p 177–183
2. A. Peker and W.L. Johnson, A Highly Processable Metallic Glass: Zr41.2Ti 13.8Cu12.5Ni10.0Be22.5, *Appl. Phys. Lett.*, 1993, **63**, p 2342–2344
3. A. Inoue, Stabilization of Metallic Supercooled Liquid and Bulk Amorphous Alloys, *Acta Mater.*, 2000, **48**, p 279–306
4. A. Inoue and N. Nishiyama, New Bulk Metallic Glasses for Applications as Magnetic-Sensing, Chemical, and Structural Materials, *MRS Bull.*, 2007, **32**, p 651–657
5. H.A. Bruck, T. Christman, A.J. Rosakis, and W.L. Johnson, Quasi-Static Constitutive Behavior of $Zr_{41.25}Ti_{13.75}Ni_{10}Cu_{12.5}Be_{22.5}$ Bulk Amorphous Alloys, *Scripta Metall. Mater.*, 1994, **30**, p 429–434
6. W. Löser, J. Das, A. Güth, H.-J. Klauß, C. Mickel, U. Kühn, J. Eckert, S.K. Roy, and L. Schultz, Effect of Casting Conditions on Dendrite-Amorphous/Nanocrystalline Zr-Nb-Cu-Ni-Al In Situ Composites, *Intermetallics*, 2004, **12**, p 1153–1158
7. U. Kühn, J. Eckert, N. Mattern, and L. Schultz, ZrNbCuNiAl Bulk Metallic Glass Matrix Composites Containing Dendritic bcc Phase Precipitates, *Appl. Phys. Lett.*, 2002, **80**, p 2478–2480

8. J. Das, A. Güth, H.-J. Klauss, C. Mickel, W. Löser, J. Eckert, S.K. Roy, and L. Schultz, Effect of Casting Conditions on Microstructure and Mechanical Properties of High-Strength Zr73.5Nb9Cu7Ni 1Al9.5 In Situ Composites, *Scripta Mater.*, 2003, **49**, p 1189–1195
9. J. Das, W. Löser, U. Kühn, J. Eckert, S.K. Roy, and L. Schultz, High-Strength Zr-Nb-(Cu, Ni, Al) Composites with Enhanced Plasticity, *Appl. Phys. Lett.*, 2003, **82**, p 4690–4692
10. J. Eckert, U. Kühn, J. Das, S. Scudino, and N. Radtke, Nanostructured Composite Materials with Improved Deformation Behavior, *Adv. Eng. Mater.*, 2005, **7**, p 587–596
11. J. Eckert, He. Guo, J. Das, and W. Löser, Nanostructured Composites in Multicomponent Alloy Systems, *Mater. Trans.*, 2003, **44**, p 1999–2006
12. L.Q. Xing, Y. Li, K.T. Ramesh, J. Li, and T.C. Hufnagel, Enhanced Plastic Strain in Zr-Based Bulk Amorphous Alloys, *Phys. Rev.*, 2001, **B 64**, p 1802011
13. J. Schroers and W.L. Johnson, Ductile Bulk Metallic Glass, *Phys. Rev. Lett.*, 2004, **93**, p 255506
14. J. Das, M.B. Tang, K.B. Kim, R. Theissmann, F. Baier, W.H. Wang, and J. Eckert, "Work Hardenable" Ductile Bulk Metallic Glass, *Phys. Rev. Lett.*, 2005, **94**, p 205501–205504
15. Y.F. Sun, B.C. Wei, Y.R. Wang, W.H. Li, T.L. Cheung, and C.H. Shek, Plasticity-Improved Zr–Cu–Al Bulk Metallic Glass Matrix Composites Containing Martensite Phase, *Appl. Phys. Lett.*, 2005, **87**, p 051905
16. J. Das, K.B. Kim, W. Xu, B.C. Wei, Z.F. Zhang, W.H. Wang, S. Yi a, and J. Eckert, Ductile Metallic Glasses in Supercooled Martensitic Alloys, *Mater. Trans.*, 2006, **47**, p 2606–2609
17. P. Yu, H.Y. Bai, M.B. Tang, and W.L. Wang, Excellent Glass-Forming Ability in Simple $Cu_{50}Zr_{50}$-Based Alloys, *J. Non-Cryst. Solids*, 2005, **351**, p 1328–1332
18. Z.W. Zhu, S.J. Zheng, H.F. Zhang, B.Z. Ding, Z.Q. Hu, P.K. Liaw, Y.D. Wang, and Y. Ren, Plasticity of Bulk Metallic Glasses Improved by Controlling the Solidification Condition, *J. Mater. Res.*, 2008, **23**, p 941–948
19. J. Eckert, J. Das, K.B. Kim, F. Baier, M.B. Tang, W.H. Wang, and Z.F. Zhang, High Strength Ductile Cu-Base Metallic Glass, *Intermetallics*, 2006, **14**, p 876–881
20. S. Pauly, J. Das, C. Duhamel, and J. Eckert, Martensite Formation in a Ductile Cu47.5Zr47.5Al5 Bulk Metallic Glass Composite, *Adv. Eng. Mater.*, 2007, **9**, p 487–491
21. J. Das, S. Pauly, C. Duhamel, B.C. Wei, and J. Eckert, Microstructure and Mechanical Properties of Slowly Cooled Cu47.5Zr47.5Al5, *J. Mater. Res.*, 2007, **22**, p 326–333
22. T.B. Massalski, *Binary Alloy Phase Diagrams*, 2nd ed., ASM International, Metals Park, OH, 1990
23. K.S. Lee, H.-J. Jun, S. Pauly, B. Bartusch, Y.W. Chang, and J. Eckert, Thermomechanical Characterization of $Cu_{47.5}Zr_{47.5}Al_5$ Bulk Metallic Glass Within the Homogeneous Flow Regime, *Intermetallics*, 2009, **17**, p 65–71
24. F. Jiang, Z.B. Zhang, L. He, J. Sun, H. Zhang, and Z.F. Zhang, The Effect of Primary Crystallizing Phases on Mechanical Properties of $Cu_{46}Zr_{47}Al_7$ Bulk Metallic Glass Composites, *J. Mater. Res.*, 2006, **21**, p 2638–2645
25. J. Das, S. Pauly, M. Boström, K. Durst, M. Göken, and J. Eckert, Designing Bulk Metallic Glass and Glass Matrix Composites in Martensitic Alloys, *J. Alloys Compd.*, 2009, **483**, p 97–101
26. J.J. Lewandowski, W.H. Wang, and A.L. Greer, Intrinsic Plasticity or Brittleness of Metallic Glasses, *Philos. Mag. Lett.*, 2005, **85**, p 77–87
27. W. Hoyer and R. Jödicke, Short-range and Medium-Range Order in Liquid Au-Ge alloys, *J. Non-Cryst. Solids*, 1995, **102**, p 102–105
28. V. Simonet, F. Hippert, M. Audier, and R. Bellissent, Local Order in Liquids Forming Quasicrystals and Approximant Phases, *Phys. Rev.*, 2001, **65**, p 024203
29. J.F. Loffler, Bulk Metallic Glasses, *Intermetallics*, 2003, **11**, p 529–540
30. A. Inoue, T. Shibat, and T. Zhang, Effect of Additional Elements On Glass Transition Behavior And Glass Formation Tendency of Zr-Al-Cu-Ni alloys, *Mater. Trans.*, 1995, **36**, p 1420–1426
31. J.T. Fan, F.F. Wu, Z.F. Zhang, F. Jiang, J. Sun, and S.X. Mao, Effect of Microstructures on the Compressive Deformation and Fracture Behaviors of $Zr_{47}Cu_{46}Al_7$ Bulk Metallic Glass Composites, *J. Non-Cryst. Solids*, 2007, **353**, p 4707–4717
32. D.C. Qiao, G.J. Fan, P.K. Liaw, and H. Choo, Fatigue Behaviors of the $Cu_{47.5}Zr_{47.5}Al_5$ Bulk-Metallic Glass (BMG) and $Cu_{47.5}Zr_{38}Hf_{9.5}Al_5$ BMG Composite, *Int. J. Fatigue*, 2007, **29**, p 2152–2154
33. K.M. Flores, W.L. Johnson, and R.H. Dauskardt, Fracture and Fatigue Behavior of a Zr–Ti–Nb Ductile Phase Reinforced Bulk Metallic Glass Matrix Composite, *Scripta Mater.*, 2003, **49**, p 1181–1187
34. M. Kusy, U. Kühn, A. Concustell, A. Gebert, J. Das, J. Eckert, L. Schultz, and M.D. Baro, Fracture Surface Morphology of Compressed Bulk Metallic Glass-Matrix-Composites and Bulk Metallic Glass, *Intermetallics*, 2006, **14**, p 982–986
35. K.M. Flores and R.H. Dauskardt, Fracture and Deformation of Bulk Metallic Glasses and Their Composites, *Intermetallics*, 2004, **12**, p 1025–1029
36. T.A. Baser, J. Das, J. Eckert, and M. Baricco, Glass Formation and Mechanical Properties of $(Cu_{50}Zr_{50})_{100-x}Al_x$ (x = 0, 4, 5, 7) Bulk Metallic Glasses, *J. Alloys Compd.*, 2008, **483**, p 146–149